Tribol Lett (2015) 57:21
DOI 10.1007/s11249-014-0458-1

ORIGINAL PAPER

Influence of Subsurface Micro/Nano-Structural Evolution on Macroscopic Tribological Behavior of Ni_3Al Matrix Composites

Qingshuai Zhu · Xiaoliang Shi · Wenzheng Zhai · Kang Yang · Ahmed Mohamed Mahmoud Ibrahim · Zengshi Xu · Long Chen · Yecheng Xiao · Ao Zhang · Qiaoxin Zhang

Received: 30 October 2014 / Accepted: 22 December 2014 / Published online: 23 January 2015
© Springer Science+Business Media New York 2015

Abstract The relationship between macroscopic tribological behavior and subsurface micro/nano-structural evolution needs to be studied in detail. We report here the results of dry sliding tribological tests of Ni_3Al matrix composites with 1.5 wt% graphene nanoplatelets (GNPs) under different loads. We found that the friction coefficient decreased with increasing load, while the wear rate showed a downward trend after an initial increase. During the sliding wear process, severe plastic deformation and an accumulation of friction heat caused the formation of an ultrafine layer (UL) and a matrix refinement layer (MRL). The UL contributes to the reduction of friction coefficient and wear rate, and the MRL contributes to the improvement of wear resistance. In addition, GNPs accumulating in the UL tend to be parallel to the worn surface, causing a reduction in friction and an increase in wear resistance for the properties of easily shearing off and high tensile strength. The hardness and elastic modulus of the UL and MRL increased due to grain refinement and the accumulation of GNPs in these layers. The effective hardness of the multilayer was approximately 7.2 GPa.

Keywords Wear mechanisms · Solid lubrication mechanisms · Nanotribology · Solid lubrication film thickness

1 Introduction

Liquid lubricants fail to work effectively and coatings have limited service life under extreme working conditions [1]. These disadvantages have driven scientists to search for new lubricants, among which are the metallic matrix self-lubricating composites, which have been found to have excellent mechanical and tribological properties. Experimental evidence suggests that at room temperature Ni_3Al-based alloys have a high melting point, low density, and good oxidation resistance, but a poor plasticity, and that at high temperature, they have low strength [2, 3]. However, it has also been shown that the ductility of Ni_3Al can be greatly improved by the addition of small amounts of boron (B) [4] and that chromium (Cr) as a reinforcement can greatly promote the strength and improve the tribological performance of Ni_3Al at high temperature due to the formation of chromates as high-temperature solid lubricants [5, 6]. Therefore, Ni_3Al-based self-lubricating composites under dry sliding conditions are worth further study due to their potential to meet the demands of advanced technological systems, such as solid self-lubricating bearings, high-performance gas turbine engines, and aerospace applications.

The subsurface micro/nano-structure has also been proven to have a great effect on the tribological performance of Ni_3Al-based self-lubricating composites [7, 8], with the smooth and two-layer structure, denoted the friction layer, having an important influence on their excellent friction properties [7]. Tribological performance also largely depends on the average thickness of each layer, but is more dependent on the thickness of the bonded layer [8]. In their investigation of the effect of silver (Ag) and Ti_3SiC_2 on the tribological properties of TiAl-matrix self-lubricating composites at room and increased temperatures, Xu

---

Q. Zhu · X. Shi (✉) · W. Zhai · K. Yang · A. M. M. Ibrahim · Z. Xu · L. Chen · Y. Xiao · A. Zhang · Q. Zhang
School of Mechanical and Electronic Engineering, Wuhan University of Technology, 122 Luoshi Road, Wuhan 430070, China
e-mail: sxl071932@126.com

et al. [9] observed that the composition of the multilayer also impacts on the friction and wear performance.

In the search for the perfect lubricant which provides the lowest friction and wear, graphene, a crystallographically perfect film of graphitic carbon, has also been investigated [10–13]. The structure and mechanical properties of graphene have been reviewed by Yong et al. [10], who reported that graphene possesses excellent mechanical properties, such as high levels of stiffness and strength. The single-layered graphene has also been found to exhibit a Young's modulus of ~1,100 GPa and a tensile strength of 130 GPa [11–13]. Graphene nanoplatelets (GNPs) are multilayer particles consisting of 10–30 sheets of graphene that largely retain single-layer properties [14]. This property has led GNPs to be widely used as reinforcing filler to prevent deformation [15]. In addition, tribological studies also suggest that GNPs shear off and weld at a higher load and that they provide a lubricating effect [16].

The aim of the study reported here was to further investigate the impact of subsurface micro/nano-structure on the macroscopic tribological behavior of Ni_3Al-matrix composites (NMCs) with the addition of 1.5 wt% GNPs under different average Hertz stresses. The existential state and action mechanism of GNPs were also studied. Several analytical techniques are used to gain an understanding of the morphology of the worn surface and layer formation and to study the structure, composition and thickness of the subsurface layer with the purpose to correlate them with the macroscopic tribological behavior of NMCs.

2 Experimental Details

The NMCs used in this study were fabricated by spark plasma sintering (SPS). The composite powders of the Ni_3Al matrix consist of commercially available nickel (Ni), aluminum (Al), Cr, molybdenum (Mo), zirconium (Zr), and B powders (average size 30–50 µm, 99.9 wt% in purity) at te atomic ratio of 4.5 Ni:0.333 Cr:0.243 Mo:0.0047 Zr:0.0015 B. Commercially available GNPs with an average thickness of 5–15 nm and 0.5–20 µm in lateral dimension (Nanjing XFNANO Materials Tech Co., Ltd., Nanjing, China) were used. The weight fraction of the graphene nanoplates in the NMCs is 1.5 wt%. Before the SPS process, the raw powders were mixed by vibration milling at a vibration frequency of 45 Hz. Vials are composed of Teflon. After being mixed and dried, the mixtures were sintered by SPS using a D.R. Sinter® SPS3.20 apparatus (Sumitomo Coal & Mining, now SPS Syntex Inc., Japan) at 1,150 °C under a pressure of 30 MPa for 6 min in a pure argon (Ar) atmosphere protection. The heating rate was 100 °C/min. The as-prepared specimen surfaces were ground to remove the layer on the surface and polished mechanically, first with emery papers down to 1,200 grit and then with 0.05-µm wet polishing diamond pastes until the arithmetical mean deviation of the profile of NMCs reached 0.05 µm. The GCr15 steel balls were purchased with the arithmetical mean deviation of the profile of 0.01 µm.

Vicker's [17] hardness of each as-received specimen was measured according to the ASTM standard E92-82, using a HVS-1000 Vicker's hardness instrument with a load of 1 kg and a dwell time of 10 s. The test was carried out at ten locations to contradict the possible effect of an indenter resting on the harder reinforcement particles. The density of each as-prepared specimen was determined using Archimedes' method according to the ASTM Standard B962-08 [18]. Five tests were conducted and the average value recorded. The chemical composition and physical and mechanical properties of NMCs and the GCr15 steel balls are listed in Table 1.

The dry sliding friction and wear tests were conducted on a HT-1000 ball-on-disc high-temperature tribometer (Zhong Ke Kai Hua Corp., China) according to the ASTM Standard G99-95 [19]. The disc samples of NMCs were rotated and slid against a stationary ball slider (diameter 6 mm) under the following conditions: sliding speed of 0.24 m/s, room temperature, and relative humidity of about 65 %. The friction radius was 2 mm, and the testing time was 80 min. The contact loads were 1.65, 2.15, 3.65, 6.65, 9.65, 11.65, 13.65, and 16.65 N. The average Hertz stress and contact width for the ball-on-disc configuration with a different contact load are shown in Table 2. The friction coefficient was automatically measured and recorded in real time by the computer system of the friction tester. The wear volume was determined as $V = A \times L$, where A is the average value of cross-section area of worn scar (see Fig. 1b), and L is the perimeter of the worn scar. The wear rate $W = V/(S \times N)$, is calculated as a function of the wear volume divided by the sliding distance S and the applied load N, and expressed in units of cubic millimeter per applied load per meter ($mm^3\ N^{-1}\ m^{-1}$). The tests for each tested conditions were repeated three times to obtain reliable data and the average value used as the data for further evaluation.

X-ray diffraction studies with CuKα radiation at 30 kV and 40 mA at a scanning speed of $0.01°\ s^{-1}$ were carried out on the as-prepared composites to analyze the phase compositions. As shown in Fig. 2, the as-prepared NMCs were mainly composed of the Ni_3Al phase and the peaks were present at 2θ, which is equal to about 24°, 36°, 43°, 51°, and 75°.

The morphology and microstructure of GNPs and the fractured surface of NMCs were characterized by field emission scanning electron microscopy (FESEM; Zeiss Ultra Plus; Carl Zeiss Group, Jena, Germany) for the

Table 1 Chemical compositions, physical and mechanical properties of Ni_3Al-matrix composites and GCr15 steel

Material	Composition	Density (g/cm^3)	Vickers hardness (GPa)
NMCs	Ni_3Al + 1.5 wt% GNPs	7.6	5.8
GCr15 steel	Iron carbon (1.05 wt% C, 1.4 wt% Cr)	7.85	6.9

NMC, Ni_3Al-matrix composite; GNP, graphene nanoplatelet; Cr, chromium

Table 2 Static Hertz pressure and contact width for the ball-on-disc configuration under different loads

Hertz stress/contact width	Load (*N*)							
	1.65	2.15	3.65	6.65	9.65	11.65	13.65	16.65
Average Hertz stress (MPa)	211	231	276	338	383	408	431	460
Contact width (mm)	0.035	0.038	0.046	0.056	0.063	0.067	0.071	0.076

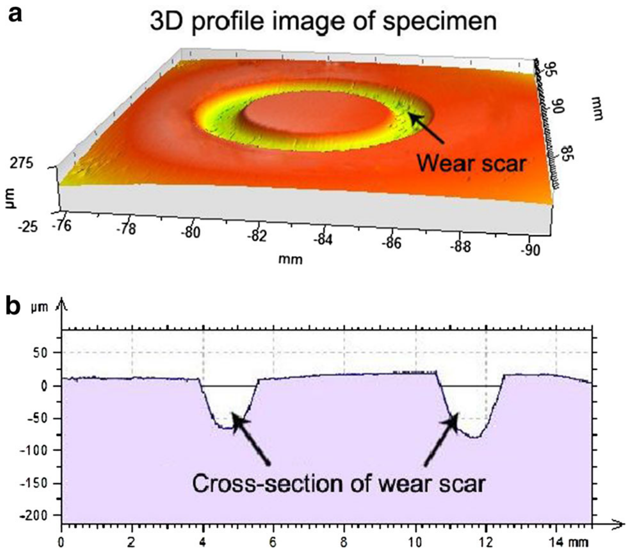

Fig. 1 Three-dimensional (*3D*) profile images of the worn surface of the specimen sliding against GCr15 steel

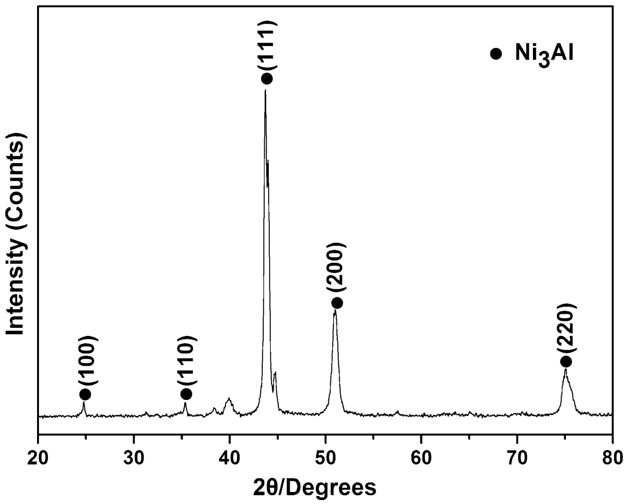

Fig. 2 X-ray diffraction (*XRD*) pattern of the as-prepared Ni_3Al-matrix composites (*NMCs*)

investigation of wear mechanisms. As shown in Fig. 3a, the as-received GNPs are stacks of multi-layer graphene sheets, including platelet morphology. The high-magnification image of the area enclosed by the rectangle in Fig. 3a is shown in Fig. 3b. Figure 3c shows the cross-section of NMCs; the high-magnification image of the area enclosed by the rectangle in Fig. 3c is shown in Fig. 3d. As shown in Fig. 3c, d, the GNPs are wrinkled and curled, but they still retain their platelet shape in the NMCs. These bends are the result of the high pressure experienced during the SPS processing [16]. The addition of GNPs is expected to improve the mechanical and tribological performance of NMCs [15, 16].

The worn surfaces of NMCs were analyzed using a JXA-8230 SuperProbe Electron Probe Microanalyser [electron probe microanalysis; JEOL Ltd., Tokyo, Japan) to understand the wear mechanism of the surface of NMCs. We also characterized the cross-section of the worn scars of NMCs by FESEM and energy dispersive spectroscopy (EDS; Inca X-Act; Oxford Instruments, Abingdon, UK) to gain an understanding of the formation mechanism of the subsurface layer. For analyzing the microstructure changes which are accompanied by the formation of the subsurface layer, such as grain size, grain boundary orientation, and special grain boundary, among others, we undertook electron back-scattered diffraction (EBSD) on a Nordlys EBSD detector with a Peltier cooled CCD camera, with an operating voltage of 20 kV and an acquisition speed of

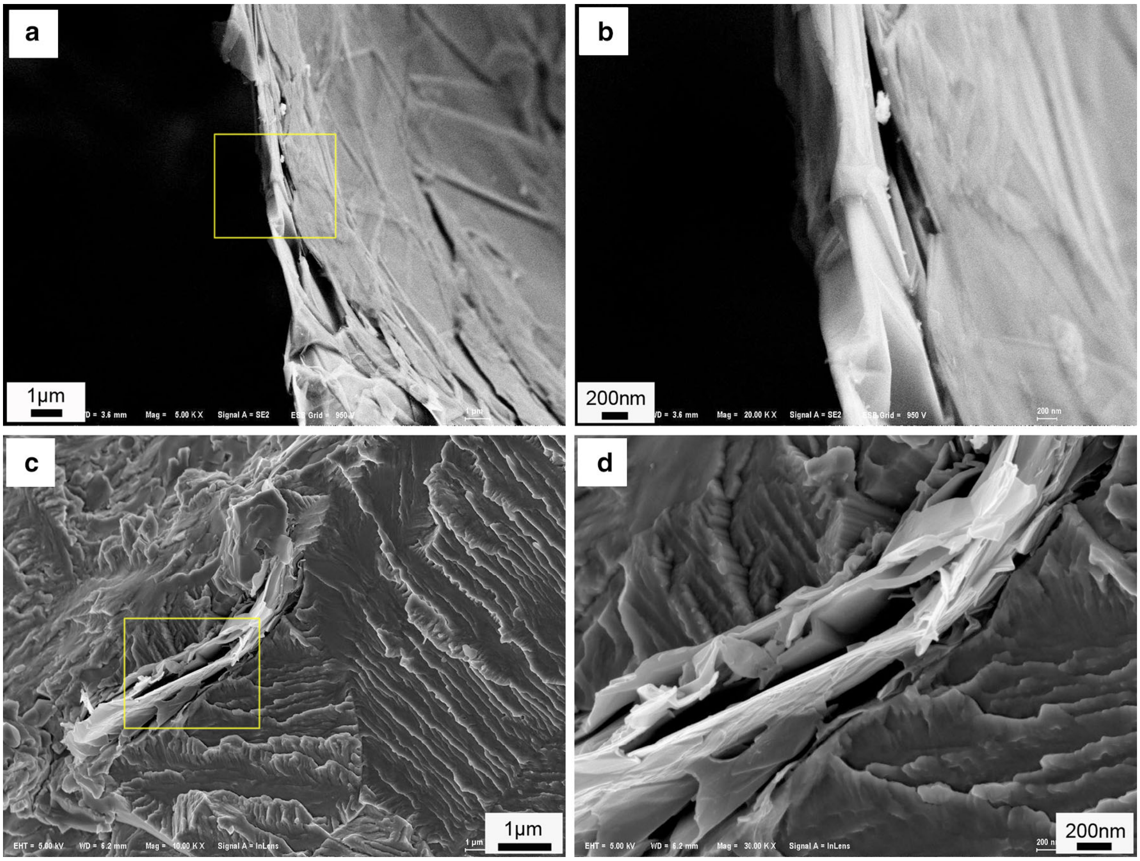

Fig. 3 **a** Typical field emission scanning electron microscopy (FESEM) images of the graphene nanoplatelets (GNPs), **b** high-magnification image of area enclosed by the *rectangle* in **a** **c** cross-section of NMCs, **d** high-magnification image of area enclosed by the *rectangle* in (**c**)

288.16 Hz. A stepsize of 0.2 μm was maintained constant for the map. The area of the EBSD map of the subsurface under the worn surface was 60 × 100 μm^2. To calculate the hardness and elastic modulus of the different layers, we made nanoindentations at the peak load of 8,000 μN using a nanomechanical test instrument (Hysitron, Inc., Eden Praire, MN).

3 Results and Discussion

3.1 Tribological Performance

Figure 4 shows the wear rate of GCr15 steel versus load dependence. Five tests were conducted and the average value obtained. As shown in Fig. 4, the wear rate initially increases to a maximum value (4.8×10^{-6} $mm^3\ N^{-1}\ m^{-1}$) from the minimum value (2.9×10^{-6} $mm^3\ N^{-1}\ m^{-1}$), and then slowly decreases to a relatively stable value (about 4.0×10^{-6} $mm^3\ N^{-1}\ m^{-1}$) along with the increase in load.

Figure 5 shows the friction coefficient and wear rate of NMCs versus load dependence, with the the friction coefficient decreasing with increasing load. The wear rate of NMCs can be seen to have the similar trend as the wear rate of GCr15 steel shown in Fig. 4, with an initial increase to a maximum value (5.3×10^{-5} $mm^3\ N^{-1}\ m^{-1}$) from the minimum value (3.0×10^{-5} $mm^3\ N^{-1}\ m^{-1}$), followed by a slow decrease to a relatively stable value (about

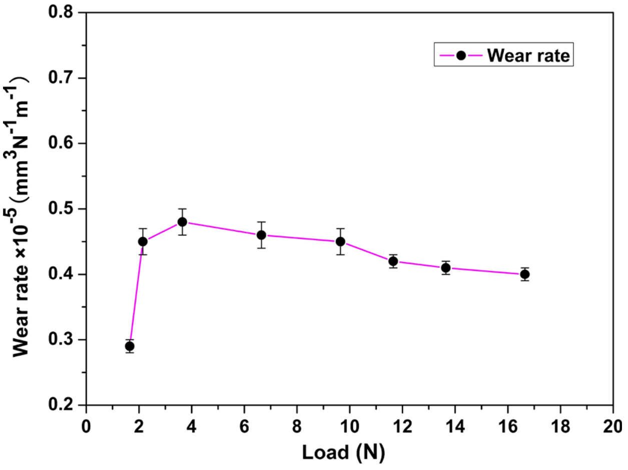

Fig. 4 The wear rate of GCr15 steel versus load dependence

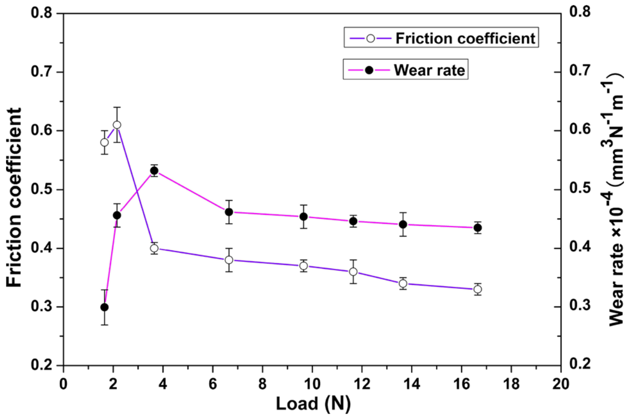

Fig. 5 The friction coefficient and wear rate of NMCs versus load dependence

4.5×10^{-5} mm^3 N^{-1} m^{-1}) along with increasing load. This trend may be due to the formation of the micro/nano-structure under the worn surface under different contact stress. To obtain a clear understanding of the effect of evolution of subsurface micro/nano-structure on the tribological performance of NMCs, we selected three worn scars under loads of 1.65, 3.65 and 16.65 N for comparative analysis.

Figure 6 shows the typical morphologies of worn surfaces of NMCs under loads of 1.65, 3.65 and 16.65 N, respectively. Many deep scratches and furrows in the sliding direction are visible in Fig. 6a, illustrating that the main wear mechanism of NMCs under a load of 1.65 N is severe abrasive wear. In comparison, the morphology of the worn surface shown in Fig. 6b undoubtedly shows that material has been peeled off in an messy way even though a multilayer structure did form under the worn surface. However, as shown in Fig. 6c, the worn surface of NMCs under a load 16.65 N is completely flat and smooth, which may account for the great tribological performance.

Figure 7 shows the typical morphologies of worn surfaces of GCr15 steel under loads of 1.65 N (Fig. 7a), 3.65 N (Fig. 7b), and 16.65 N (Fig. 7c). The EDS analysis [recorded as the mean value of three measurements + standard deviation for all elements] of the elements (wt%) was also used to investigate the composition of the worn surfaces of GC15 steel. The worn surface of GCr15 steel under 1.65 N has many hard protrusions, which will partially become embedded in the counterface and scratch and/or groove the softer surface of NMCs. The worn surface of GCr15 steel under 3.65 N is uneven and covered with white solid material. The EDS analysis results show that the area shown in area B (Fig. 7b) contains a large amount of Ni and Al, illustrating that there is element transfer when NMCs slide against GCr15 steel under a load of 3.65 N. In contrast, under a load of 16.65 N, the worn surface of GCr15 steel is much smoother and has a small number of of furrows and scratches. Based on this analysis, the morphologies of the worn surface of GCr15 steel are good agreement with the phenomenon shown in Fig. 6. EDS analysis (the mean value of three measurements and standard deviation for all elements) of elements (wt.%) is also used to investigate the compositions of the worn surfaces of GC15 steel. The results show that the area A (in Fig. 7a) and C (in Fig. 7c) contain hardly any Ni and Al, while area B (in Fig. 7b) contains a large mount of Ni and Al, illustrating that there is element transfer when NMCs slide against GCr15 steel under 3.65 N.

3.2 Subsurface morphology of NMCs

To gain further understanding of the reason for differences in macroscopic tribological behavior, we performed analysis using FESEM and EBSD. Figure 8 shows the FESEM images of cross-sections of worn scars of NMCs under 1.65 and 3.65 N. As shown in Fig. 8a, no obvious delamination is formed in the cross-section, and the worn surface is largely rugged with a lot of loose wear debris. A crack strip (oval in Fig. 8a, b) can also be found under the worn surface. In Fig. 8b, clear delamination can be identified; note that the cross-section has been divided into three layers, namely, the ultrafine layer (UL) (Fig. 8b, I), the matrix refinement layer (MRL) (Fig. 8b, J), and the substrate of NMCs (Fig. 8b, K). In addition, many more crack strips (oval) can be seen under the worn surface.

It would appear that delamination occurs under a higher average Hertz stress. Combined with the tribology performance shown in Fig. 5, it is possible that the delamination structure may result in lower friction coefficients but higher wear rates. On the one hand, layer I would be harder than the original substrate because of the grain refinement, which in turn would prevent the hard protrusions of GCr15 steel from being pressed into the substrate and thereby reduce the plastic deformation such as the deep furrows and scratches formed at the effect of cyclic shear strain. Moreover, plastic deformation has been shown to be the main energy dissipation mechanism of metal friction pairs [15]. Therefore, the UL could attribute to the lower friction coefficient and lower wear rate. On the other hand, the development of subsurface crack nucleation caused by stress concentration could result in the formation of microcracks in the cross-section and ultimately lead to delamination. Under a higher average Hertz stress, the microcracks may continue to expand to cracks that then contribute to the particle shedding, as shown in Fig. 6b. In this case, the existence of the MRL is rather precarious and it cannot play a stable role in preventing cracks from extending to the worn surface, leading to the higher wear rates.

However, as shown in Fig. 5, both the friction coefficient and the wear rate decrease in a stepwise manner with

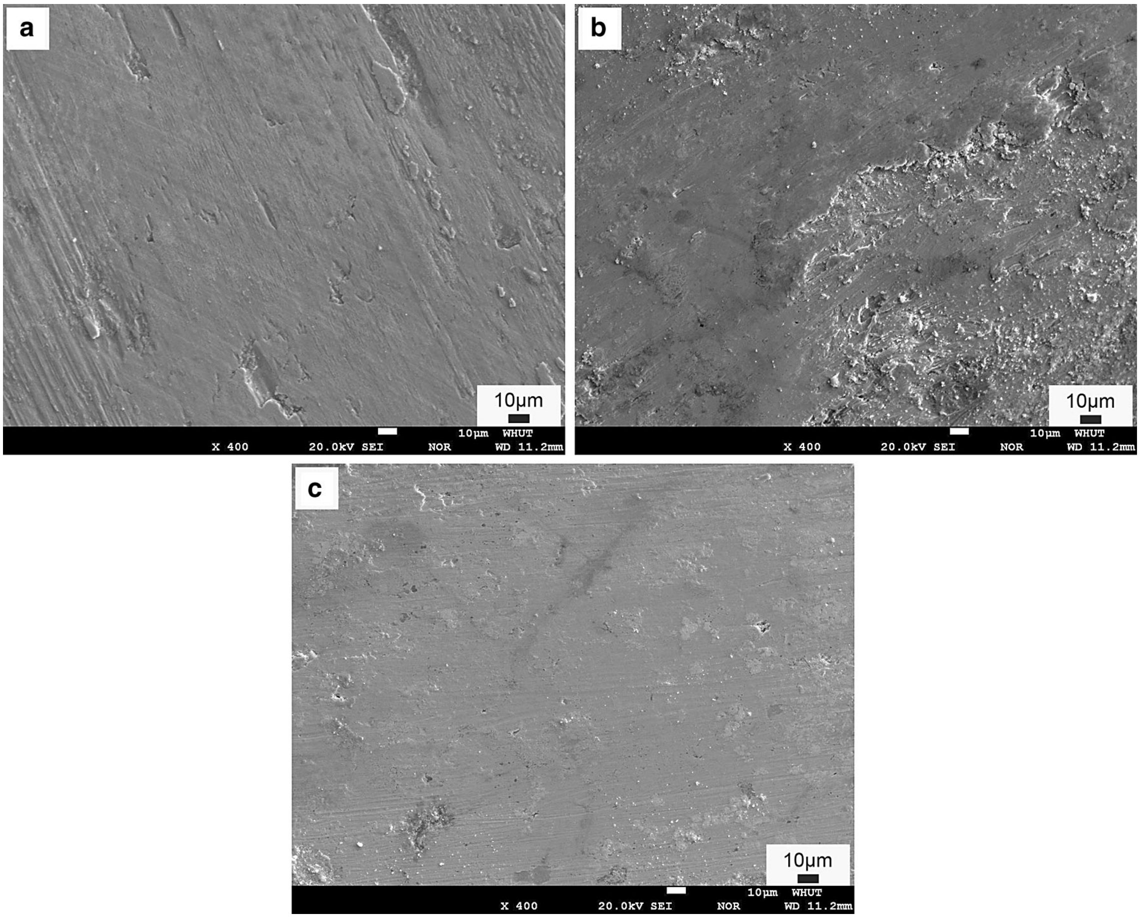

Fig. 6 The typical morphologies of worn surfaces of NMCs under loads of 1.65 N (**a**), 3.65 N (**b**), and 16.65 N (**c**)

increasing average Hertz stress. To further our understanding of this phenomenon, we investigated images of cross-sections of worn scars formed under a load of 16.65 N by FESEM (Fig. 9). High-magnification images of Fig. 9a are shown in Fig. 9b, c. In Fig. 9a, b, delamination (L, M and N) similar to that in Fig. 8b (load of 3.65 N) also occurs in the cross-section of NMCs under a load of 16.65 N. The difference is that under a load of 16.65, the thickness of L is about 4 μm and the thickness of M is about 5 μm, illustrating that the UL and MRL formed under a load of 16.65 N are thicker than those formed under a load of 1.65 and 3.65 N, respectively. Somekawa et al. [20] investigated the effect of grain refinement on the fracture toughness and fracture mechanism and found that grain refinement improved the fracture toughness and restrained the generation and extension of cracks. From our analysis, it can be concluded that UL contributes to a reduction in the friction coefficient and to an increase in wear resistance increasing and that MRL contributes to a lower wear rate.

EDS analysis (recorded as the mean value of three measurements + standard deviation for all elements) of elements (wt%) in areas marked by rectangles (A, B, C) in Fig. 9a are listed in Table 3. It can be found that the content of C in area A is more than that in area B, while the content of C in area C is the least. Therefore, the EDS analysis results show that C element exhibits enrichment in the UL and MRL. GNPs have been used as an effective reinforcing filler to prevent deformation [15]. Therefore, layer L, which is relatively thicker and contains more GNPs, would be sufficiently hard to protect the surface from damage, such as furrows and scratches, resulting in the lower friction coefficient. In addition, the GNPs in layer M can also contribute to the prevention of crack propagation and reduce particle shedding. The GNPs (encircled by the virtual yellow oval) in layers M and N are bevelled at an angle of 45° with the worn surface. However, the GNPs in layer L are finer and almost parallel to the worn surface, as shown in Fig. 9c. Under the condition that the GNPs in layer L are bevalled at the angle of 45° with the worn surface in Fig. 9a, they will prevent the hard protrusions pressed into the substrate from turning into furrows and scratches by generating a strong resistance due to their high levels of stiffness and strength, resulting in higher wear resistance at the cost of a clear reduction in lubricity. While

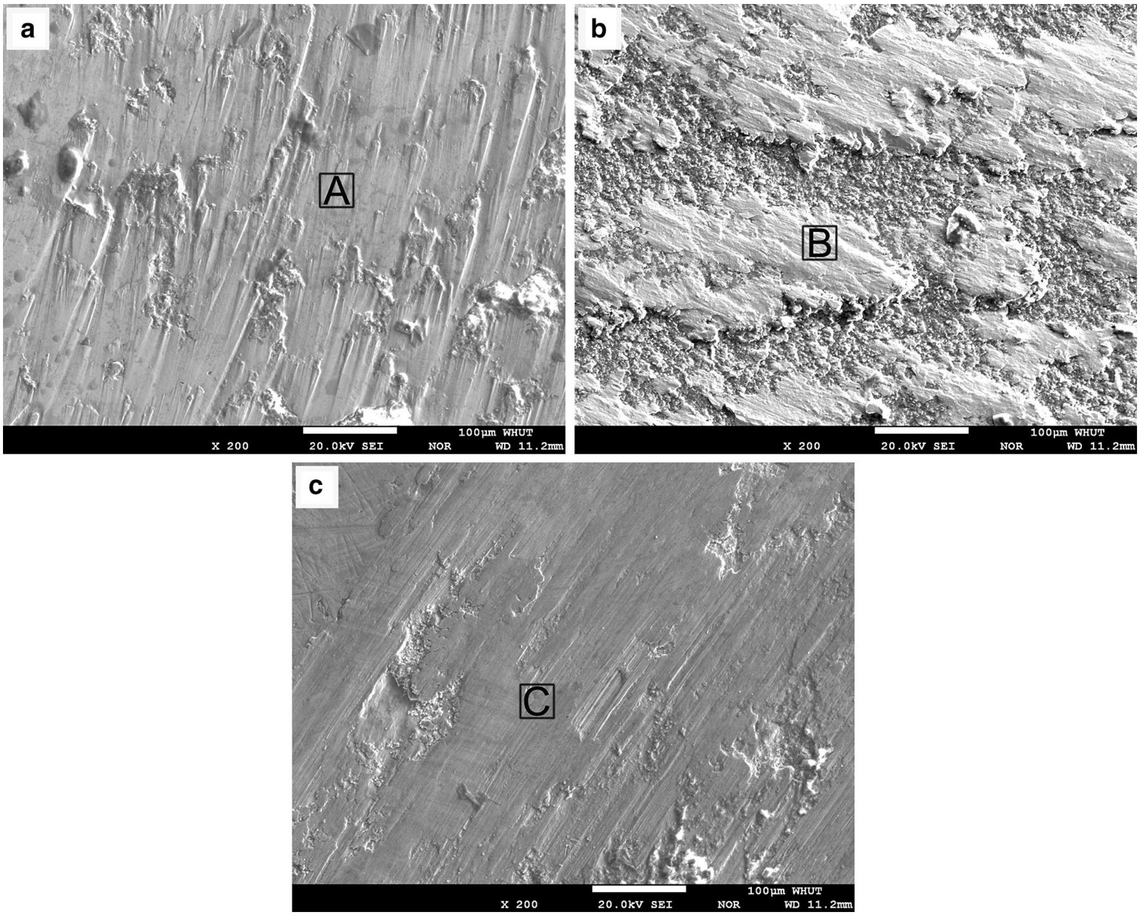

Fig. 7 The typical morphologies of worn surfaces of GCr15 steel under loads of 1.65 N (**a**), 3.65 N (**b**), and 16.65 N (**c**), respectively

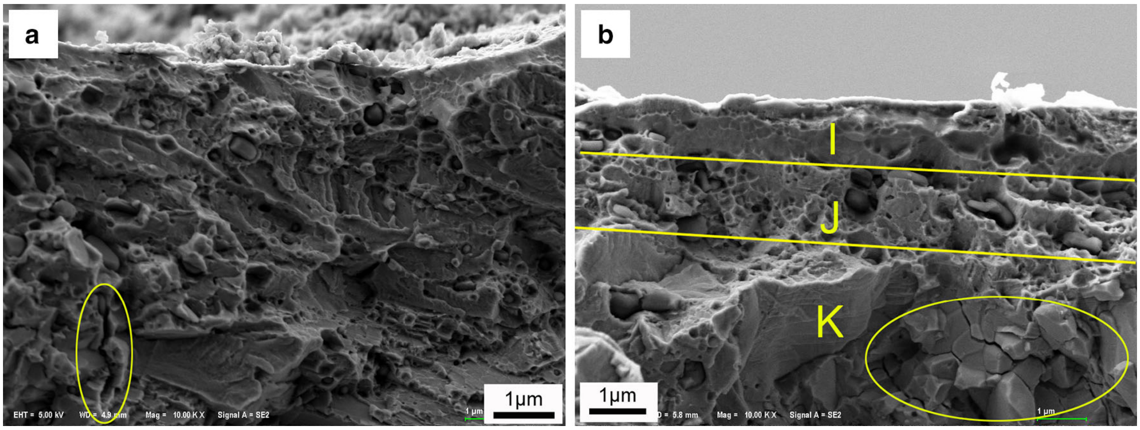

Fig. 8 FESEM images of cross-sections of wear scars of NMCs under loads of 1.65 N (**a**) and 3.65 N (**b**). See text for explanation of I, J, K and of the circle

GNPs in layer L are parallel to the worn surface, they will prevent the hard protrusions from being pressed into the substrate and easily sheared at the interface of graphene layers [7]. As a consequence, the unique self-organization microstructures of GNPs can improve the mechanical and tribological properties of UL, making a significant contribution to the anti-wear and anti-friction properties.

Figure 10 shows the characterization of NMCs near to the worn surface under a load of16.65 N investigated using EBSD. The phase distribution of GNPs is marked in gray,

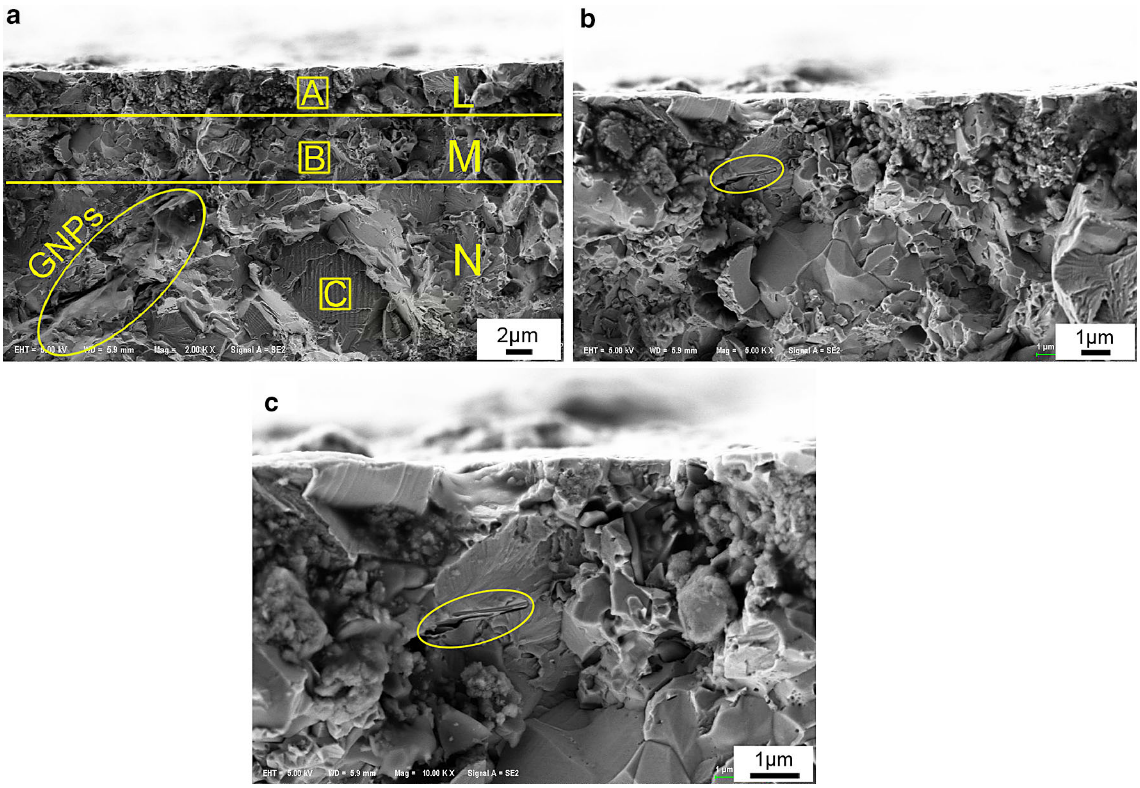

Fig. 9 FESEM images of the cross-section of a worn scar formed under a load of 16.65 N (**a**), and its high-magnification images (**b**) and (**c**). See text for explanation of L, M, and N

Table 3 Energy dispersive spectroscopy analysis results (wt%) of areas A, B, and C in Fig. 9a

Area in Fig. 9a	Elements (wt%)						
	Carbon	Oxygen	Aluminum	Nickel	Chromium	Molybdenum	Iron
A	2.76	0.72	8.76	76.20	4.78	4.41	2.37
B	2.35	–	9.39	79.48	3.82	4.96	–
C	1.63	–	8.21	81.13	4.48	4.55	–

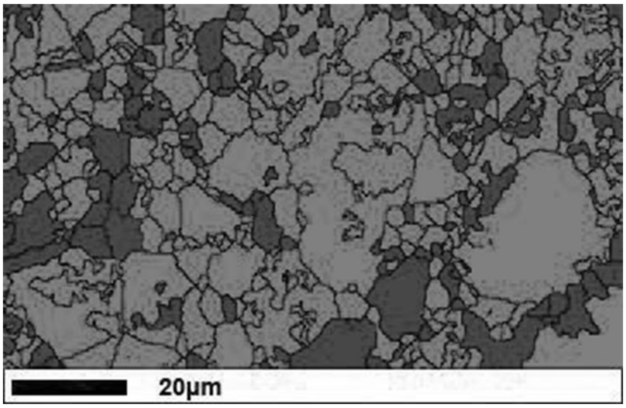

Fig. 10 Characterization of NMCs near the worn surface under a load of 16.65 N analyzed by energy dispersive spectroscopy

and the phase distribution of Ni_3Al is marked in black. The phase distribution indicates that: (1) GNPs and Ni_3Al near to the worn surface exhibit refinement; (2) GNPs accumule near the worn surface. The results are in good agreement with the those shown in Fig. 9b and with the EDS analysis in Table 3. Figure 11a shows the grain orientation according to the inverse pole figure of GNPs (Fig. 11b) and Ni_3Al (Fig. 11c). As shown in Fig. 11a, GNPs near the worn surface exhibit the same or a similar orientation, which is in good agreement with the results shown in Fig. 9b, c.

Figure 12 shows the frequency of misorientation angle distribution in UL and MRL. The theoretical misorientation angle distribution of the indexed region is marked by red curve, and the black curve correlates to the actual misorientation angle distribution. As shown in Fig. 12, the actual misorientation distribution in the low-angle range is approximately consistent with the theoretical curve. The actual misorientation angles are mainly about 57° and 71°. These results illustrate that the accumulation of dislocation occurs during the sliding process, which may help to

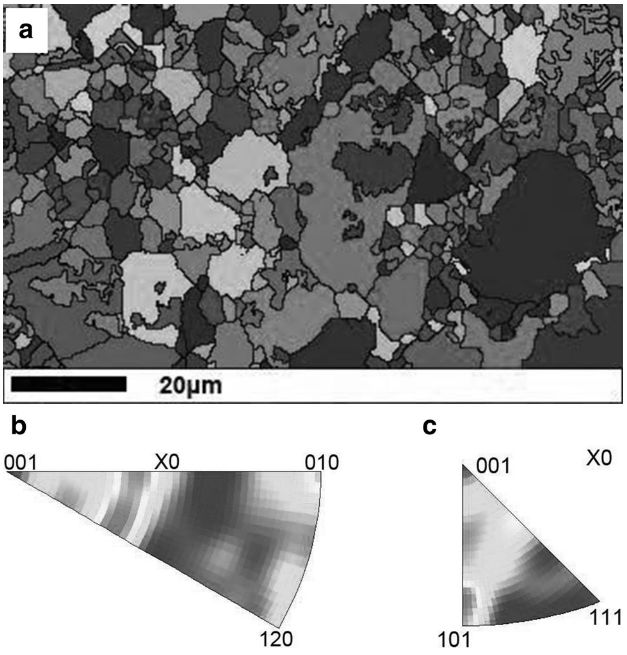

Fig. 11 The EBSD orientation map (**a**), according to the inverse pole figure of GNPs (**b**) and the inverse pole figure of Ni_3Al (**c**)

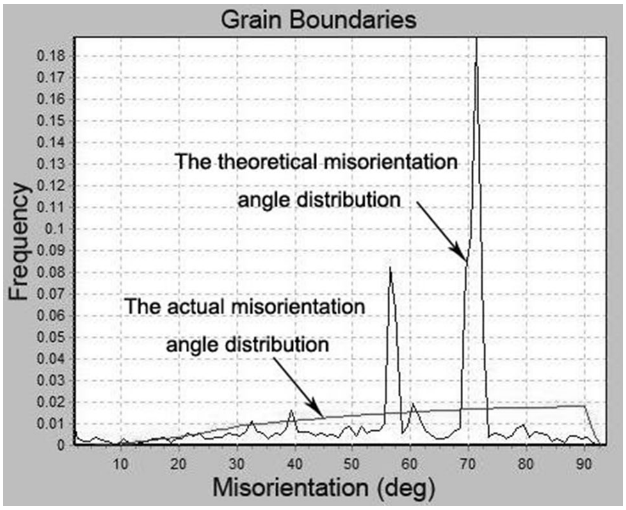

Fig. 12 The frequency of misorientation angle distribution in the ultrafine and matrix refinement layers. See text for definition of curves

transform a substantial part of the small-angle grain boundaries into large-angle grain boundaries.

The above analysis shows that grain refinement is a significant factor for the evolution of micro/nano-structure and one of the most important factors for the improvement of friction and wear properties under the larger average Hertz stress. Dynamic recrystallization caused by plastic deformation and temperature is thought to be the major causes of grain refinement [21, 22].

On the one hand, Onions et al. [23] found that when the plasticity index was >0.45, plastic deformation would inevitably occur no matter how low the load was. They define the plasticity index (ψ) by surface peak height standard deviation (σ) and correlation length (β^*) as:

$$\psi = \frac{E^*}{H} \times \frac{\sigma}{\beta^*} \tag{1}$$

$$\frac{1}{E^*} = \frac{1 - v_1^2}{E_1} + \frac{1 - v_2^2}{E_2} \tag{2}$$

$$\sigma^2 = \sigma_1^2 + \sigma_2^2 \tag{3}$$

$$\frac{1}{\beta^*} = \frac{1}{\beta_1^*} + \frac{1}{\beta_2^*} \tag{4}$$

where H is the hardness of specimen, and E^* is composite modulus estimated by Eq. (2)—of which E_1 and v_1 are the elastic modulus and Poisson ratio of the specimen, respectively; E_2 and v_2 are the elastic modulus and Poisson ratio of the counterface ball. σ is calculated by Eq. (3)—of which σ_1 and σ_2 are the surface peak height standard deviation of the specimen and counterface ball, respectively. In our study, the specimen is NMCs and the counterface ball is the GCr15 steel ball. β^* is determined by Eq. (4)—of which β_1^* and β_2^* are the correlation lengths of the rough surface of specimen and counterface ball, respectively. In addition, it has been widely thought that the structure of a surface polished by emery paper is subject to generalized Gaussian distribution [24, 25]. Therefore, σ_1 and σ_2 can be calculated by:

$$\sigma_1 = 1.25R_{a1} \tag{5}$$

$$\sigma_2 = 1.25R_{a2} \tag{6}$$

where R_{a1} (0.05 μm) and R_{a2} (0.01 μm) mentioned in the experimental details are the arithmetical mean deviation of the profile of the specimen and counterface ball. The value of σ_1 and σ_2, corresponding to the R_{a1} and R_{a2} of generalized Gaussian distribution, are 0.88 and 0.13 μm, respectively. The value of the other material parameters used in the equations above are based on reported data [26, 27] and are provided in Table 4. The calculated results show that the plasticity index (ψ) equals 10.63, which is much larger than 0.45. Therefore, it can be concluded that NMCs will develop with severe plastic deformation.

On the other hand, dynamic recrystallization can be divided into discontinuous dynamic recrystallization (dDRX) and continuous dynamic recrystallization (cDRX) [28]. The process of dDRX is accomplished through nucleation and growth of the recrystallized grain to eliminate the defects caused by deformation, such as dislocation and sub-grain boundary, which is characterized by the migration of large-angle grain boundary [29]. The severe plastic deformation and higher temperature are necessary to the appearance of dDRX [30, 31]. Therefore, we now discuss the temperature of the surface of NMCs caused by

Table 4 Material parameters for NMCs and GCr15 steel

Parameter	Symbol	Value
Surface peak height standard deviation of NMCs	R_{a1}	0.05 μm
Correlation length of NMCs	β_1^*	0.88 μm
Surface peak height standard deviation of GCr15 steel	R_{a2}	0.01 μm
Correlation length of GCr15 steel	β_2^*	0.13 μm
Hardness of NMCs	H	5.8 GPa
elastic modulus of NMCs	E_1	178 GPa
Poisson ratio of NMCs	v_1	0.34
elastic modulus of GCr15 steel	E_2	219 GPa
Poisson ratio of GCr15 steel	v_2	0.3

the accumulation of friction heat. The local surface temperature (T) can be determined according to Rupert and Schuh [32]:

$$T = \frac{Q_A}{h_s}\left\{1 - \operatorname{erfc}\left[h_s\sqrt{\frac{t}{K\rho c}}\right]\exp\left[\frac{h_s^2 t}{K\rho c}\right]\right\} \tag{7}$$

$$Q_A = \frac{\mu P v}{A_s} \tag{8}$$

where h_s is the heat transfer coefficient for convection, t is the time, and K, ρ, and c are the thermal conductivity, density, and specific heat, respectively. Q_A is the frictional heat power per unit area, which is calculated by Eq. (8)—of which μ is the friction coefficient, P is the normal load, v is the sliding velocity, and A_S is the surface area of the wear track. The thermal conductivity, specific heat, and heat transfer coefficient for convection are given by Meng et al. [33], Qiang et al. [34], and Tang et al. [35]. The values of the other material parameters, which are obtained from experimental measurements or established parameters during the sliding, are provided in Table 5. Figure 13 shows the predicted temperature as a function of sliding distance, where the value of the local surface temperature (T) after sliding 80 min is about 490 °C. However, the minimum temperature ($T_{\min}$) for dDRX is about 556 °C, which is calculated according to McQueen and Jonas [36] and Sellars [37]:

$$T_{\min} = 0.5T_m \tag{9}$$

where T_m is the melting point of the specimen, which is replaced by the melting point of Ni_3Al. Therefore, it can be concluded that the local surface temperature is too low to cause discontinuous dynamic recrystallization.

Table 5 Material parameters for NMCs

Parameter	Symbol	Value
Thermal conductivity	K	28.85 W m^{-1} K^{-1}
Density	ρ	7.6 g cm^{-3}
Specific heat	c	0.396 J g^{-1} K^{-1}
Heat transfer coefficient	h_s	30 W m^{-1} K^{-1}
Friction coefficient	μ	0.33
Normal load	P	16.65 N
Sliding velocity	v	0.24 m s^{-1}
Sliding time	t	4,800 s

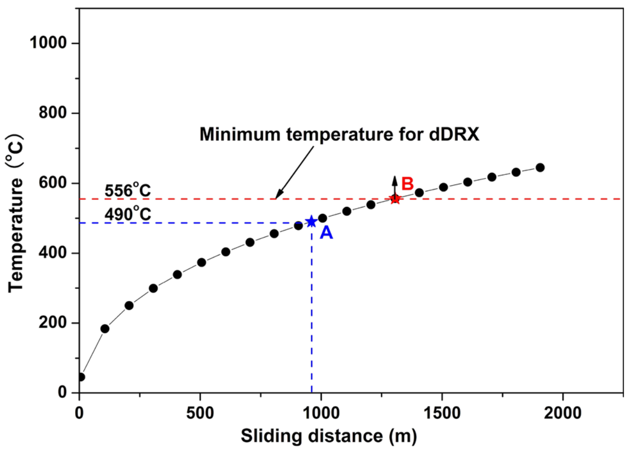

Fig. 13 Predicted temperature as a function of sliding distance

However, after years of research, it has been found that the ultrafine grained structures can be developed during the process of cDRX at severe plastic deformation but low temperature [30, 38]. During this process, sub-grains absorb the dislocations and help to transform a substantial part of the small-angle grain boundaries into large-angle grain boundaries by absorbing dislocations, thereby leading to grain refinement.

3.3 Typical mechanical properties

For further understanding the reasons of improvement of tribological properties, the effect of grain refinement on hardness and elastic modulus of UL and MRL have also been studied by nanoindentation tests. Each experiment was repeated three times in each layer to ensure statistical reliability. Figure 14 shows a FESEM image of a cross-section of NMCs after indentation where it is clearly

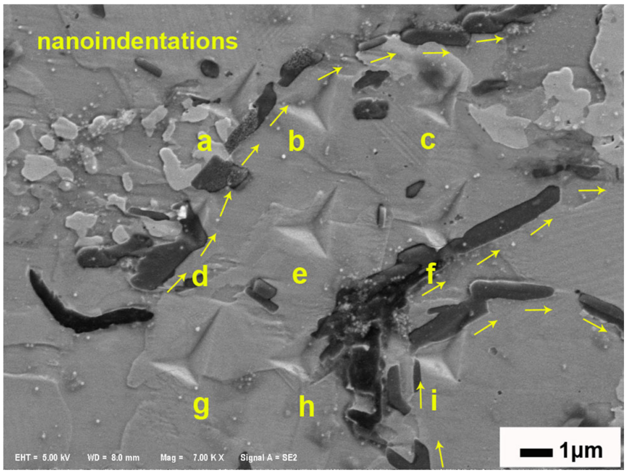

Fig. 14 FESEM image from a cross-section of NMCs after indentation

visible that GNPs migrate from the substrate to the UL and MRL, becoming fine and parallel to the worn surface under the effect of thermal stress. The arrows show the migration trajectories of GNPs. It can also been seen that indentation c in the UL is smaller than indentations a and b, that indentations d and f in the MRL are smaller than indentation e, and that indentations h and I in the substrate are slightly smaller than indentation g. A closer examination reveals the similarity between indentations c, d, h, and I is the appearance of GNPs. In addition, the average size of indentations a, b, and c in the UL is smaller than that of indentations d, e, and f in the MRL, and the average size of indentations d, e and f in the MRL is smaller than that of indentations g, h, and I in the substrate.

The force displacement curves, corresponding to indentations a–i in Fig. 14, are shown in Fig. 15. The measured values of hardness and of elastic modulus of each layer are shown in Table 6. In Fig. 15, the curves of indentations f, g, and h are not as smooth as the others and are characterized by discontinuity at certain penetration depths, referred to as the “pop-ins”. Jian et al. [39] and Lorenz et al. [40] investigated the reason for appearance of pop-ins and concluded that pop-ins are associated with the homogeneous dislocation nucleation mechanisms during nanoindentation. In addition, as shown in Table 6, the hardness value and elasticity modulus of indentations made on the GNPs, such as indentations c, d, f, h, and I, are relatively larger than those of others in the same layer. Moreover, the average hardness value and average elasticity modulus of MRL are larger than those of the substrate, while those of UL are the

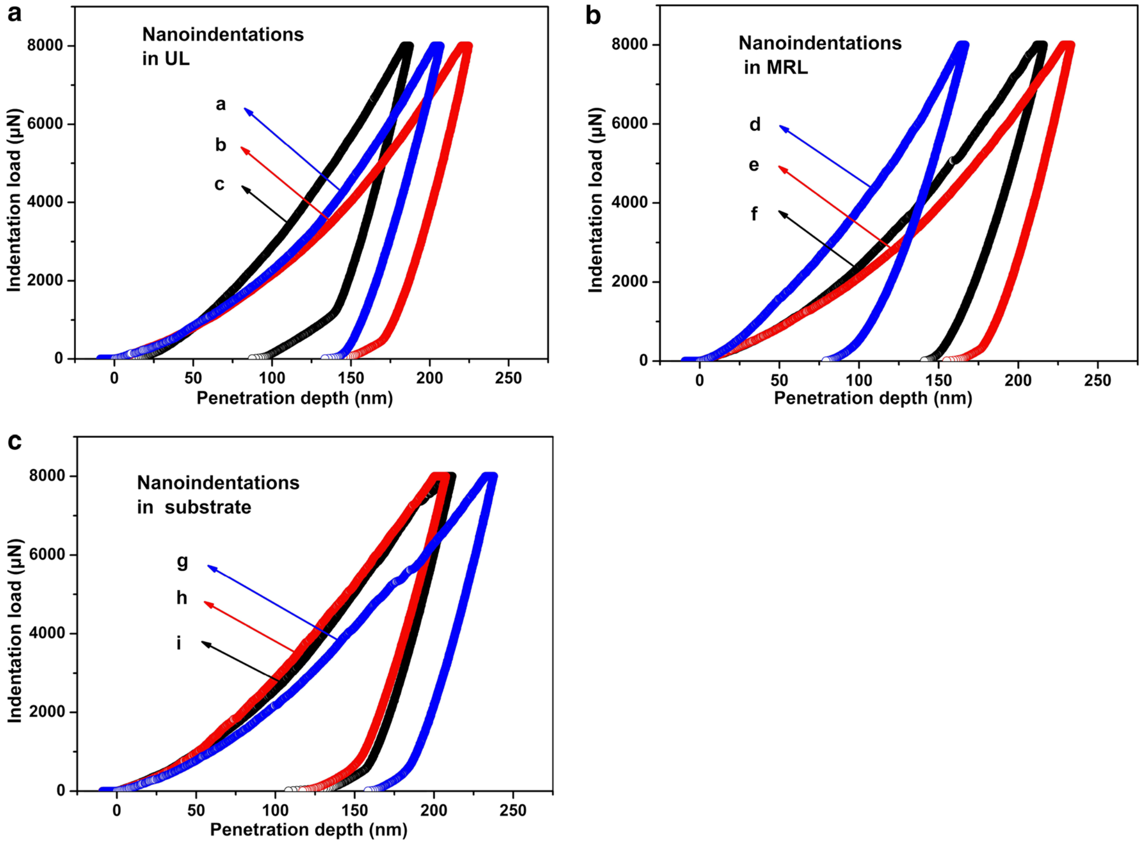

Fig. 15 The force displacement curves of indentations in the ultrafine layer (*UL*; **a**), matrix refinement layer (*MRL*, **b**), and substrate (**c**)

Table 6 The hardness and elastic modulus of each layer

Hardness and elastic modulus	Ultrafine layer[a]			Matrix refinement layer[a]			Substrate[a]		
	a	b	c	d	e	f	g	h	I
Hardness (GPa)	7.2	5.9	9.0	10.1	5.1	6.2	5.0	6.8	6.4
Average hardness (GPa)	7.4			7.1			6.1		
Elastic modulus (GPa)	179	174	195	192	170	167	166	176	180
Average elastic modulus (GPa)	183			176			174		

[a] The lowercase letters a–I refer to nanoindentations shown on Fig. 15a–c

largest of all. The results are in good agreement with those shown in Fig. 14. After studying Figs. 14 and 15 and Table 6 in detail, it can been concluded that: (1) GNPs with high levels of stiffness and strength can reinforce the substrate; (2) the MRL is harder than the substrate, while UL is the hardest due to grain refinement and the accumulation of GNPs in the UL and MRL.

The effective hardness of the multilayer (H_e) can be approximately calculated by the method of Bhattacharya and Nix [41]:

$$\frac{H_e}{H_s} = 1 + \left(\frac{H_l}{H_s} - 1\right) \exp\left[-\frac{H_l/H_s}{\left({}^{Y_l}/_{Y_s}\right) \times \left({}^{E_l}/_{E_s}\right)^{0.5}} \times \frac{h_c}{h}\right] \tag{10}$$

where E_l, Y_l, and H_l are the elastic modulus, yield strength, and hardness of the upper layer, respectively. E_s, Y_s, and H_s are the elastic modulus, yield strength, and hardness of the underlayer, respectively. h_c is the depth of indentation, which can be calculated from Fig. 15. h is the thickness of upper layer, which can be calculated from Fig. 9. Y_l and Y_s can be approximately calculated by the method of Francis [42]:

$$H_l = 2.8Y_l \tag{11}$$

$$H_s = 2.8Y_s \tag{12}$$

The value of H_e can then be calculated to be about 7.2 GPa, and the increase in local surface hardness contributes to the grain refinement caused by cDRX and the accumulation of GNPs in the thermal-stress coupled field.

4 Conclusion

Macroscopic tribological behavior and subsurface micro/nano-structure of NMCs with 1.5 wt% GNPs under loads of 1.65, 3.65, and 16.65 N have been studied in detail. The results show that the friction coefficient decreases with increasing load. However, the wear rate initially increases to a maximum value (5.3×10^{-5} mm^3 N^{-1} m^{-1}) from the minimum value (3.0×10^{-5} mm^3 N^{-1} m^{-1}) and then slowly decreases to a relatively stable value (about 4.5×10^{-5} mm^3 N^{-1} m^{-1}) together with the increase in load. Variations in macroscopic tribological behavior can be attributed to the evolution of a subsurface micro/nano-structure in the thermal-stress coupled field. Grain refinement has been found to occur in the UL and MRL during the process of cDRX, caused by severe plastic deformation and the accumulation of friction heat. Further analysis showed that UL can reduce plastic deformation, such as severe abrasive wear, which is the main energy dissipation mechanism on the worn surface, thus contributing to the reduction of friction coefficient and wear rate; the stable MRL can restrain the generation and extension of cracks, thus contributing to the increase of wear resistance. In addition, the GNPs accumulating in the UL tend to be parallel to the worn surface and allow an improvement in friction reduction and wear-resistance for the properties of easily shearing off and high tensile strength. The hardness and elastic modulus of the UL and MRL were found to increase due to grain refinement and the accumulation of GNPs in them, and the effective hardness of the multilayer is approximately 7.2 GPa. Overall, the influence of subsurface micro/nano-structural evolutions on macroscopic tribological behavior in the thermal-stress coupled field was studied in this paper and requires further analysis in the future.

Acknowledgments This work was supported by the Project for Science and Technology Plan of Wuhan City (2013010501010139); the National Natural Science Foundation of China (51275370); the Fundamental Research Funds for the Central Universities (2014-yb-004). The authors also wish to express their gratitude our colleagues at the Material Research and Testing Center of Wuhan University of Technology for their assistance.

References

1. Karin, G., Luo, H.L., Feng, D., Li, C.H.: Ni_3Al-based intermetallic alloys as a new type of high-temperature and wear-resistant materials. J. Iron. Steel Res. Int. **14**, 21–25 (2007)

2. Fujii, H., Nakajima, K., Goto, A.: Infiltration and combustion synthesis of an intermetallic compound Ni_3Al. Mater. Sci. Eng., A **223**, 21–28 (1997)
3. Huang, B., Xiong, W.H., Yang, Q.Q., Yao, Z.H., Zhang, G.P.: Preparation, microstructure and mechanical properties of multi-component Ni_3Al-bonded cermets. Ceram. Int. **40**, 14073–14081 (2014)
4. Chaki, T.K.: Boron in polycrystalline Ni_3Al-mechanism of enhancement of ductility and reduction of environmental embrittlement. Mater. Sci. Eng., A **190**, 109–116 (1995)
5. Zhu, S.Y., Bi, Q.L., Yang, J., Liu, W.M.: Influence of Cr content on tribological properties of Ni_3Al matrix high temperature self-lubricating composites. Tribol. Int. **44**, 1182–1187 (2011)
6. Karin, G., Luo, H.L., Feng, D., Li, C.H.: Wear of Ni_3Al-based materials and its chromium-carbide reinforced composites. Wear **265**, 1751–1755 (2008)
7. Stadler, Z., Krnel, K., Kova, J., Kosma, T.: Tribochemical reactions on sliding surface of the sintered metallic brake linings against SiC ceramic brake disk. Wear **292–293**, 232–238 (2012)
8. Kato, T., Kawaguchi, M., Sajjad, M.M., Choi, J.: Friction and durability characteristics of ultrathin perfluoropolyether lubricant film composed of bonded and mobile molecular layers on diamond-like carbon surfaces. Wear **257**, 909–915 (2004)
9. Xu, Z.S., Shi, X.L., Wang, M., Zhai, W.Z., Yao, J., Song, S.Y., Zhang, Q.X.: Effect of Ag and Ti_3SiC_2 on tribological properties of TiAl matrix self-lubricating composites at room and increased temperatures. Tribol. Lett. **53**, 617–629 (2014)
10. Yong, R.J., Kinloch, I.A., Gong, L., Novoselov, K.S.: The mechanics of graphene nanocomposites: a review. Compos. Sci. Technol. **72**, 1459–1476 (2012)
11. Zhang, S.L., Li, Y.M., Pan, N.: Graphene based supercapacitor fabricated by vacuum filtration deposition. J. Power Sour **206**, 476–482 (2012)
12. Zhang, K., Zhang, L.L., Zhao, X.S., Wu, J.S.: Graphene/polyaniline nanofiber composites as supercapacitor electrodes. Chem. Mater. **22**, 1392–1401 (2010)
13. Balandin, A.A., Ghosh, S., Bao, W.Z., Calizo, I., Teweldebrhan, D., Miao, F., Lau, C.N.: Superior thermal conductivity of single-layer graphene. Nano Lett. **8**, 902–907 (2008)
14. Berman, D., Erdemir, A., Sumant, A.V.: Reduced wear and friction enabled by graphene layers on sliding steel surfaces in dry nitrogen. Carbon **59**, 167–175 (2013)
15. Belmonte, M., Ramirez, C., González-Julián, J., Schneider, J., Miranzo, P., Osendi, M.I.: The beneficial effect of graphene nanofillers on the tribological performance of ceramics. Carbon **61**, 431–435 (2013)
16. Nieto, A., Lahiri, D., Agarwal, A.: Synthesis and properties of bulk graphene nanoplatelets consolidated by spark plasma sintering. Carbon **50**, 4068–4077 (2012)
17. ASTM Standards E92-82: Standard Test Method for Vickers Hardness of Metallic Materials. ASTM Int, West Conshohocken (2003)
18. ASTM Standards B962-08: Standard Test Methods for Density of Compacted or Sintered Powder Metallurgy (PM) Products Using Archimedes' Principle. ASTM Int, West Conshohocken (2008)
19. ASTM Standards G99-95: Standard Test Method for Wear Testing With a Pin-on-Disk Apparatus. ASTM Int, West Conshohocken (1995)
20. Somekawa, H., Mukai, T.: Effect of grain refinement on fracture toughness in extruded pure magnesium. Scripta Mater. **53**, 1059–1064 (2005)
21. Xu, X.F., Zhao, Y.G., Ma, B.D., Zhang, J.T., Zhang, M.: Rapid grain refinement of 2024 Al alloy through recrystallization induced by electropulsing. Mater. Sci. Eng., A **612**, 223–226 (2014)
22. Huang, J., Xu, Z.: Evolution mechanism of grain refinement based on dynamic recrystallization in multiaxially forged austenite. Mater. Lett. **60**, 1854–1858 (2006)
23. Onions, R.A., Archard, J.F.: The contact of surfaces having a random structure. J. Phys. D Appl. Phys. **6**, 289–304 (1973)
24. Cogdell, J.D.: A convolved multi-Gaussian probability distribution for surface topography applications. Precis. Eng. **32**, 34–46 (2008)
25. Liu, Y., Jian, W., Wang, J.Y., Hofmann, S., Kovac, J.: Influence of non-Gaussian roughness on sputter depth profiles. Appl. Surf. Sci. **276**, 447–453 (2013)
26. Raju, S.V., Oni, A.A., Godwal, B.K., Yan, J., Drozd, V., Srinivasarr, S., Lebeau, J.M., Rajan, K., Saxena, S.K.: Effect of B and Cr on elastic strength and crystal structure of Ni_3Al alloys under high pressure. J. Alloys Compd. (2015). doi:10.1016/j.jallcom.2014.09.012
27. Qin, M., Zhang, Y.Z., Zhu, J., Luo, X.: The effect of dynamic frictional heating on the dry sliding behaviors of M2 steel against GCr15 steel. Wear **261**, 767–772 (2006)
28. Sakai, T., Belyakov, A., Kaibyshev, R., Miura, H., Jonas, J.J.: Dynamic and post-dynamic recrystallization under hot, cold and severe plastic deformation conditions. Prog. Mater Sci. **60**, 130–207 (2014)
29. Engler, O., Huh, M.Y.: Evolution of the cube texture in high purity aluminum capacitor foils by continuous recrystallization and subsequent grain growth. Mater. Sci. Eng., A **271**, 371–381 (1999)
30. Schindler, I., Macháček, J., Spittel, M.: Recrystallization in as-cast polycrystalline intermetallic compound Ni_3Al. Intermetallics **7**, 83–87 (1999)
31. Polkowski, W., Wik, P.J., Bojar, Z.: EBSD and X-ray diffraction study on the recrystallization of cold rolled Ni_3Al based intermetallic alloy. J. Alloys Compd. **614**, 226–233 (2014)
32. Rupert, T.J., Schuh, C.A.: Sliding wear of nanocrystalline Ni-W: structural evolution and the apparent breakdown of Archard scaling. Acta Mater. **58**, 4137–4148 (2010)
33. Meng, J., Jia, C.C., Wang, K.M.: Review of formation of Ni_3Al intermetallics compounds by mechanical alloying. Powder Metall. Tech. **24**, 299–309 (2006)
34. Li, Q., Huang, D.H., Cao, Q.L., Wang, F.H., Yang, J.S.: Thermodynamic properties of Ni_3Al under pressure via fist-principles calculations. J. At. Mol. Phys. **30**, 798–803 (2013)
35. Tang, B., Guo, Y.Q., Yu, S.L.: Study of temperature field induced by YAG laser rapid solidification treatment of intermetallics Ni_3Al. Trans. Heat Treat. **17**, 33–38 (1996)
36. McQueen, H.J., Jonas, J.J.: Recovery and recrystallization during high temperature deformation. Mater. Sci. Eng. **6**, 393–493 (1975)
37. Sellars, C.M.: Recrystallization of metals during hot deformation. Philos. Trans. R. Soc. Lond. A **288**, 147–158 (1978)
38. Sakai, T., Miura, H., Goloborodko, A., Sitdikov, O.: Continuous dynamic recrystallization during the transient severe deformation of aluminum alloy 7475. Acta Mater. **57**, 153–162 (2009)
39. Jian, S.R., Tseng, Y.C., Teng, I.J., Juang, J.Y.: Dislocation energetics and Pop-ins in AlN thin films by Berkovich nanoindentation. Materials **6**, 4259–4267 (2013)
40. Lorenz, D., Zeckzer, A., Hilpert, U., Grau, P., Johansen, H., Leipner, H.S.: Pop-in effect as homogeneous nucleation of dislocations during nanoindentation. Phys. Rev. B **67**, 172101 (2003)
41. Bhattacharya, A.K., Nix, W.D.: Analysis of elastic and plastic deformation associated with indentation testing of thin films on substrates. Int. J. Solids Struct. **24**, 1287–1298 (1988)
42. Francis, H.A.: Application of spherical indentation mechanics to reversible and irreversible contact between rough surfaces. Wear **45**, 221–269 (1977)